

---

# PHYSICS-INFORMED NEURAL NETWORKS FOR NON-NEWTONIAN FLUID THERMO-MECHANICAL PROBLEMS: AN APPLICATION TO RUBBER CALENDERING PROCESS

---

A PREPRINT

**Thi Nguyen Khoa Nguyen<sup>1,2,3</sup>, Thibault Dairay<sup>2</sup>, Raphaël Meunier<sup>2</sup>, Mathilde Mougeot<sup>1,4</sup>**

<sup>1</sup>*ENS Paris-Saclay, Centre Borelli, Gif-sur-Yvette, 91190 France*

<sup>2</sup>*Michelin, Centre de Recherche de Ladoux, Cébazat, 63118 France*

<sup>3</sup>*CEA-DAM Île-de-France, Bruyères-le-Châtel, 91680 France*

<sup>4</sup>*ENSIIE, Évry-Courcouronnes, 91000 France*

February 1, 2022

## ABSTRACT

Physics-Informed Neural Networks (PINNs) have gained much attention in various fields of engineering thanks to their capability of incorporating physical laws into the models. However, the assessment of PINNs in industrial applications involving coupling between mechanical and thermal fields is still an active research topic. In this work, we present an application of PINNs to a non-Newtonian fluid thermo-mechanical problem which is often considered in the rubber calendering process. We demonstrate the effectiveness of PINNs when dealing with inverse and ill-posed problems, which are impractical to be solved by classical numerical discretization methods. We study the impact of the placement of the sensors and the distribution of unsupervised points on the performance of PINNs in a problem of inferring hidden physical fields from some partial data. We also investigate the capability of PINNs to identify unknown physical parameters from the measurements captured by sensors. The effect of noisy measurements is also considered throughout this work. The results of this paper demonstrate that in the problem of identification, PINNs can successfully estimate the unknown parameters using only the measurements on the sensors. In ill-posed problems where boundary conditions are not completely defined, even though the placement of the sensors and the distribution of unsupervised points have a great impact on PINNs performance, we show that the algorithm is able to infer the hidden physics from local measurements.

**Keywords** Physics-informed neural networks, non-Newtonian fluid, thermo-mechanical problem.

## 1 Introduction

In the last few years, advances in deep learning have gained much attention in the field of physical modeling and engineering. There has been an increasing amount of research using deep learning methods to study the physics of systems by enforcing physical constraints, which are usually expressed by partial differential equations (PDEs), into the models [1, 2, 3, 4, 5]. Among these studies, the series of work of Karniadakis' group about Physics-Informed Neural Networks (PINNs) [1] rise as an attractive and remarkable scheme of solving forward and inverse PDEs problems using only a moderate amount of supervised data [6, 7, 8]. PINNs take advantage of both data-driven modeling and physics-based modeling to estimate the unknown physics of interest, which may be physical fields or physical parameters of a system. PINNs use neural networks as approximators and integrate the physical constraints of the systems into the cost function. The training process of PINNs tries to penalize (1) the loss on the initial/boundary condition if the problem is well-defined, (2) the loss on supervised data, which are observed solutions or measurements captured by sensors if they are available, (3) the loss on collocation data to embed the physical constraints expressed by

the governing PDEs. Thanks to their simplicity and powerful capability when dealing with forward or inverse problems, PINNs are gaining more and more attention from researchers and they are gradually being improved and extended [9, 10, 11, 12]. Thus far, the applicability of PINNs has been demonstrated in various fields of research. For example, Kissas et al. [13] employed PINNs for the modeling of cardiovascular flows, Tartakovsky et al. [14] and He et al. [15] applied PINNs to subsurface flow and transport problems. Recently, software editors (*e.g.* NVIDIA) are also showing great interest for this kind of methods [16, 17].

As far as computational fluid dynamics (CFD) is concerned, there has been a growing number of studies that focus on the capability of PINNs to infer the solution or estimate unknown physical parameters in problems of fluid mechanics ([18, 19, 20]). Raissi et al. [18] employed a method that used PINNs to infer hidden physics states including the velocity and pressure fields from partial knowledge of a relevant variable (the concentration field in their work) by using the governing physical laws. This work demonstrated the effectiveness of PINNs to solve inverse problems and inspired many applications ([17, 21, 22, 23, 24]). Rao et al. [19] proposed a new scheme for PINNs to model incompressible laminar fluid flows without using any supervised measurements. Reys et al. [20] used PINNs to estimate the viscosity of non-Newtonian fluid flow by using only velocity measurements. Recently, [25] proposed the non-Newtonian PINNs for complex fluid flows with different non-Newtonian constitutive models. Through these previous studies, PINNs have shown a promising power to deal with ill-posed inverse problems with multi-physics features.

In the industrial context, we often dispose of data that are captured from sensors. However, the impact of the location of these sensors on the performance of PINNs has not been paid much attention to. This is a crucial question in industrial use cases as the supervised measurements, which mostly depend on the placement of the sensors, are not randomly or uniformly distributed but only located at specific positions. Moreover, the distribution of unsupervised points (or collocation points) also plays an important role in the training process as the PDE residual is evaluated at these points. In most existing applications of PINNs, these collocation points are often chosen randomly inside the domain or generated using a Latin Hypercube Sampling strategy, which may cause large errors on the prediction at the points of discontinuity or at high gradient locations. This opens the opportunity to improve the accuracy of PINNs by taking the collocation points from some mesh that provides an *a priori* knowledge on the location of discontinuity or high gradient location (*e.g.* finite element mesh).

In this paper, we introduce a novel application of PINNs to infer the solution and identify unknown physical parameters in a non-Newtonian fluid thermo-mechanical problem. We consider an incompressible non-Newtonian fluid flow that is governed by a generalized Stokes equation coupled with a heat transfer equation. This set of PDEs is commonly used to model rubber manufacturing processes in the tire industry. First, we assess the performance of PINNs using virtual sensors coming from an industrial calendering problem simulation. To this end, we study the influence of the location of sensors and the distribution of unsupervised data on the accuracy of PINNs prediction in an ill-posed problem, where boundary conditions are not completely defined. More precisely, we suppose that only the measurements for the temperature are captured by the sensors, we aim to infer the velocity, the pressure, and the temperature at all points in the domain. Then, we examine the capability of PINNs to estimate unknown physical parameters from noisy measurements in an inverse problem. All our results are compared to a reference solution obtained by an in-house finite element solver.

The following of this paper is organized as follows. In section 2, we briefly review the framework of PINNs and their scope of use. We then study the influence of the position of supervised and unsupervised data on the accuracy of PINNs to solve a thermo-mechanical rubber calendering problem in section 3. The effect of noisy measurements is also investigated in this section. Finally, we summarize the conclusions in section 4.

## 2 Physics-Informed Neural Networks

In this section, we briefly present the framework of Physics-Informed Neural Networks (PINNs). PINNs aim at solving three main classes of problems: forward problems, inverse problems, and ill-posed problems for PDEs. For the forward problems the governing equations are known, *i.e.* the physics laws (*i.e.* PDEs with boundary/initial conditions), and the physical parameters are well-defined. In this case, the goal is to infer the solution of the PDEs. For the inverse problems, some measurements for the PDEs solutions are available and some physical parameters are unknown. The goal is to identify the values of unknown parameters. For ill-posed problems, partial data associated with the PDEs solutions are available, but the initial and/or boundary conditions are not well-defined, and the purpose is to infer all the physical fields of interest.

To illustrate the methodology of PINNs, let us consider the following parameterized PDE defined on the domain  $\Omega \subset \mathbb{R}^d$  with the boundary  $\partial\Omega$ :

$$\begin{aligned} \mathbf{u}_t + \mathcal{N}_{\mathbf{x}}(\mathbf{u}, \boldsymbol{\lambda}) &= 0, \text{ for } \mathbf{x} \in \Omega, t \in [0, T] \\ \mathcal{B}(\mathbf{u}, \mathbf{x}, t) &= 0, \text{ for } \mathbf{x} \in \partial\Omega \\ \mathbf{u}(\mathbf{x}, 0) &= g(\mathbf{x}), \text{ for } \mathbf{x} \in \Omega \end{aligned}$$

where  $\mathbf{x} \in \mathbb{R}^d$  and  $t$  are the spatial and temporal coordinates,  $\mathcal{N}_{\mathbf{x}}$  is a differential operator,  $\boldsymbol{\lambda}$  is the PDE parameter,  $\mathbf{u}$  is the solution of the PDE with initial condition  $g(\mathbf{x})$  and boundary condition  $\mathcal{B}$ , which could be Dirichlet, Neumann, Robin, or periodic boundary conditions. The subscripts denote the partial differentiation in time or space.

In the conventional framework of PINNs [1], the solution  $\mathbf{u}$  of the PDE is approximated by a fully-connected feedforward neural network  $\mathcal{NN}$ , which takes the spatial and temporal coordinates  $(\mathbf{x}, t)$  as inputs and the solution  $\mathbf{u}$  as output, given a set of supervised data. This can be represented as follows:

$$\mathbf{u} \approx \hat{\mathbf{u}} = \mathcal{NN}(\mathbf{x}, t, \boldsymbol{\theta})$$

where  $\hat{\mathbf{u}}$  denotes the prediction value for the solution and  $\boldsymbol{\theta}$  denotes the trainable parameters of the neural network. For the problems of inferring the PDE solutions, the trainable parameters  $\boldsymbol{\theta}$  are defined by the weights and the biases of the neural networks. For the problems of identification, these parameters include, in addition, the PDEs parameters that need to be defined. The parameters of the neural network are trained by minimizing the cost function  $L$ :

$$L = L_{pde} + L_{ic} + L_{bc} + L_{data} \quad (1)$$

where the terms  $L_{pde}$ ,  $L_{ic}$ ,  $L_{bc}$  and  $L_{data}$  penalize the loss in the residual of the PDE, the initial condition, the boundary condition, and the supervised data (measurements), respectively, which can be represented as follow:

$$\begin{aligned} L_{pde} &= \frac{1}{N_{pde}} \sum_{i=1}^{N_{pde}} |\hat{\mathbf{u}}_t + \mathcal{N}_{\mathbf{x}}(\hat{\mathbf{u}}, \boldsymbol{\lambda})|^2 \\ L_{ic} &= \frac{w_{ic}}{N_{ic}} \sum_{i=1}^{N_{ic}} |\hat{\mathbf{u}}(\mathbf{x}_i, 0) - g(\mathbf{x}_i)|^2 \\ L_{bc} &= \frac{w_{bc}}{N_{bc}} \sum_{i=1}^{N_{bc}} |\mathcal{B}(\hat{\mathbf{u}}, \mathbf{x}, t)|^2 \\ L_{data} &= \frac{w_{data}}{N_{data}} \sum_{i=1}^{N_{data}} |\hat{\mathbf{u}}(\mathbf{x}_i, t_i) - \mathbf{u}(\mathbf{x}_i, t_i)|^2 \end{aligned}$$

where  $N_{ic}$ ,  $N_{bc}$ ,  $N_{data}$  denote the number of learning points for the initial condition, boundary condition, and measurements, respectively, and  $N_{pde}$  denote the number of residual points (or collocation points or unsupervised points) of the PDE.  $w_{ic}$ ,  $w_{bc}$  and  $w_{data}$  are the weight coefficients for different loss terms, which are used to adjust the contribution of each term to the cost function. These coefficients can be either pre-specified before the training or tuned during the training. Recently, many studies aim at improving the efficiency of PINNs by using adaptive weights in the cost function [10, 12, 26]. We note that the number  $N_{data}$  depends on the supervised data while the numbers  $N_{ic}$ ,  $N_{bc}$  (if the initial and boundary conditions are well-defined) and  $N_{pde}$  are user-defined. To construct the residual loss  $L_{pde}$ , automatic differentiation (AD) [27] is used to compute the partial derivatives of the output  $\hat{\mathbf{u}}$  of the network with respect to the inputs  $(\mathbf{x}, t)$ . AD builds a computation graph to calculate the gradients numerically. The benefit of using AD to compute the derivatives is that we do not need to discretize the domain, which is essential in classical numerical methods.

The definition of the loss function (1) depends on the problems. For example, for forward and well-posed problems where the initial and boundary conditions of the PDE are well-defined, the loss term for the measurements  $L_{data}$  can be eliminated. However, for ill-posed problems, i.e. the initial and boundary conditions are unknown and the terms  $L_{ic}$ ,  $L_{bc}$  dissolve, then the term  $L_{data}$  becomes mandatory for the neural network to approximate the solutions. We also note that PINNs may provide different performances with different network initializations. Thus a common strategy, which is used throughout this work, is to train PINNs from random initialization several times (five times in our work) and then choose the model with the smallest training loss as the final solution [9].

### 3 Application to rubber calendering modeling

#### 3.1 Problem configuration

In the industry of tire manufacturing, calendering is a mechanical process used to create and assemble thin tissues of rubber. As sketched in Figure 1, during calendering, the rubber is smoothed out through several rotating cylindrical rolls. The modeling of the entire calendering process is a challenging task involving different length and time scales, different materials, and potentially 3D effects. However, for the sake of simplicity, the goal of the present study will only be to model the 2D temperature, velocity, and pressure fields inside rubber materials going through two contra-rotating rolls of the calender as depicted in Figure 2.

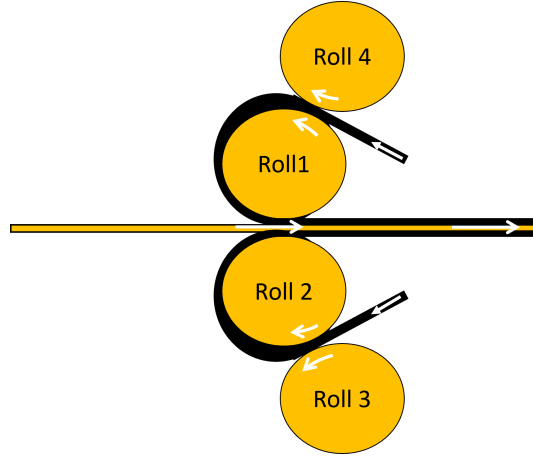


Figure 1: Sketch of a calender used to create thin tissues of rubber for tire manufacturing. The rubber material is colored in black for illustration.

The physical domain of interest together with the geometrical configuration of the study are presented in Figure 2: the 2D domain is simply bounded by an inlet, two rotating boundaries corresponding to the edges of the rolls, and an outlet. From an industrial point of view, it is of prime interest to monitor the rubber temperature inside the domain. In particular, because rubber materials are subjected to viscous heating, an important temperature elevation can be observed in highly-sheared regions (specifically at the inlet where the material can be accumulated in a rubber bead and in the very thin gap between the rolls). Such high temperatures can lead to unexpected rubber curing that could deteriorate the final material quality. In the next section, the physical equations used to model the rubber mechanical and thermal fields will be introduced.

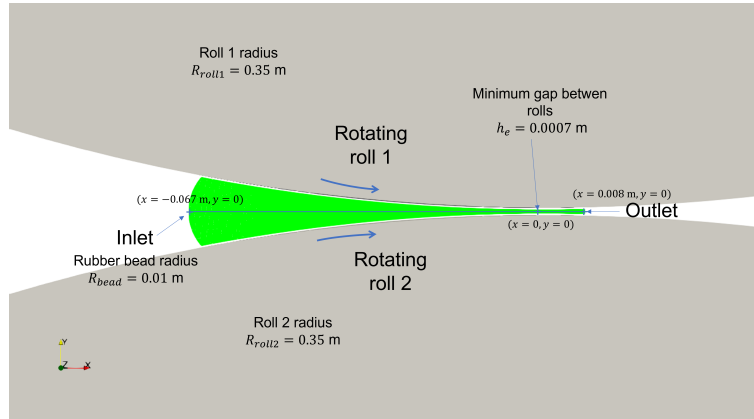


Figure 2: Sketch of the 2D configuration and geometrical setup considered in the present study. The physical domain of interest is colored in green.

### 3.2 Problem formulation

From the physical point of view, the rubber will be assimilated as an incompressible non-Newtonian fluid flow in the present study (in particular, the elastic part of the material is not considered here). Moreover, only the steady-state regime will be considered. Consequently, the equations describing the behaviour of the rubber are a generalized Stokes equation for momentum conservation, a divergence-free velocity equation for mass conservation, and a convection-diffusion equation with a viscous heating term for energy conservation. The constitutive law considered in all the presented cases is a power-law combined with an Arrhenius law to take into account the dependence of viscosity on temperature. The governing system of PDEs can be written as follows:

$$\nabla \cdot (2\eta(\vec{u}, T)\bar{\epsilon}(\vec{u})) - \vec{\nabla}p = \vec{0} \quad (2)$$

$$\nabla \cdot \vec{u} = 0 \quad (3)$$

$$\vec{u} \cdot \vec{\nabla}T = \frac{\lambda}{\rho C_p} \nabla^2 T + \frac{1}{\rho C_p} \eta(\vec{u}, T) |\gamma(\vec{u})|^2 \quad (4)$$

where  $\vec{u} = (u_x, u_y)^T$  is the velocity vector,  $p$  is the pressure,  $T$  is the temperature,  $\lambda = 20 \text{ W.m}^{-1}.\text{K}^{-1}$  is the thermal conductivity,  $\rho = 1000 \text{ kg.m}^{-3}$  is the rubber density,  $C_p = 1000 \text{ J.K}^{-1}$  is the heat capacity at 25°C. The strain-rate tensor  $\bar{\epsilon}$  is defined as:

$$\bar{\epsilon}(\vec{u}) = \frac{1}{2} \begin{pmatrix} 2\frac{\partial u_x}{\partial x} & \frac{\partial u_x}{\partial y} + \frac{\partial u_y}{\partial x} \\ \frac{\partial u_x}{\partial y} + \frac{\partial u_y}{\partial x} & 2\frac{\partial u_y}{\partial y} \end{pmatrix}$$

The dynamic viscosity  $\eta$  is defined as:

$$\eta(\vec{u}, T) = K |\tau \gamma(\vec{u})|^{n-1} \exp\left(\frac{E_\alpha}{R} \left(\frac{1}{T} - \frac{1}{T_\alpha}\right)\right)$$

where  $K = 2 \times 10^5 \text{ Pa.s}^n$  is the consistency,  $\tau = 1 \text{ s}$  is the characteristic time,  $n = 0.2$  is the power law exponent,  $E_\alpha = 7000 \text{ J.mol}^{-1}$  is the activation energy of the rubber,  $R$  is the perfect gas constant, and  $\gamma(\vec{u}) = \sqrt{2 \sum_{i,j} \bar{\epsilon}_{i,j}^2}$  is the generalized strain rate.

We consider the following quantities of reference: a length  $L_0 = 0.01 \text{ m}$ , a velocity  $u_0 = 0.5 \text{ m.s}^{-1}$ , two temperatures  $T_1 = 393.15 \text{ K}$ ,  $T_2 = 476.75 \text{ K}$ , and for the pressure, we choose  $p_0 = K \frac{u_0}{L_0} = 10^7 \text{ Pa}$ . The corresponding dimensionless variables are:  $\tilde{u}_x = \frac{u_x}{u_0}$ ,  $\tilde{u}_y = \frac{u_y}{u_0}$ ,  $\tilde{T} = \frac{T - T_1}{T_2 - T_1}$ ,  $\tilde{x} = \frac{x}{L_0}$ ,  $\tilde{y} = \frac{y}{L_0}$ . Since the dimension of the consistency  $K$  is a function of  $n$ , the quantity  $\tilde{p} = \frac{p}{p_0}$  is still a dimensional number.

The system of PDEs is rewritten as:

$$\vec{\nabla} \cdot (2\tilde{\eta}(\vec{\tilde{u}}, \tilde{T})\bar{\tilde{\epsilon}}(\vec{\tilde{u}})) - \vec{\nabla}\tilde{p} = \vec{0} \quad (5)$$

$$\vec{\nabla} \cdot \vec{\tilde{u}} = 0 \quad (6)$$

$$\vec{\tilde{u}} \cdot \vec{\nabla}\tilde{T} = \frac{1}{Pe} \vec{\nabla}^2 \tilde{T} + \frac{Br}{Pe} \tilde{\eta}(\vec{\tilde{u}}, \tilde{T}) |\tilde{\gamma}(\vec{\tilde{u}})|^2 \quad (7)$$

where the Péclet number  $Pe = \frac{\rho C_p u_0 L_0}{\lambda}$  and the Brinkman number  $Br = \frac{K u_0^2}{\lambda(T_2 - T_1)}$  are dimensionless. The dimensionless dynamic viscosity  $\tilde{\eta}$  is defined as follows:

$$\tilde{\eta}(\vec{\tilde{u}}, \tilde{T}) = |\tilde{\tau} \tilde{\gamma}(\vec{\tilde{u}})|^{n-1} \exp\left(\frac{E_\alpha}{R} \left(\frac{1}{(T_2 - T_1)\tilde{T} + T_1} - \frac{1}{T_\alpha}\right)\right)$$

For the rest of this paper, we shall only consider the dimensionless PDE system in the PINNs training process.

### 3.3 Reference solutions and validation framework

To generate reference High-Fidelity (HF) solutions of velocity, pressure, and temperature fields, the equations (5), (6), (7) are discretized and solved using an in-house generic and multi-purpose finite element solver named MEF++ and

co-developed by Laval University and Michelin [28, 29]. The velocity and temperature boundary conditions prescribed in the finite element simulation are given in Figure 3. As the first aim of this study is to assess the impact of the location of supervised points on the performance of PINNs, data captured from real sensors would be very valuable. However, obtaining different scenarios of the placement of the sensors in a real calender is an expensive and impractical process for a research study. Therefore, in our work, we use the HF solutions provided by the finite element solver as virtual measurements obtained by sensors. To evaluate the performance of PINNs, we calculate the relative  $\mathcal{L}^2$  error defined as follows:

$$\epsilon_v = \frac{\|v - \hat{v}\|^2}{\|v\|^2}$$

where  $v$  denotes the reference simulated field of interest and  $\hat{v}$  is the corresponding PINNs prediction.

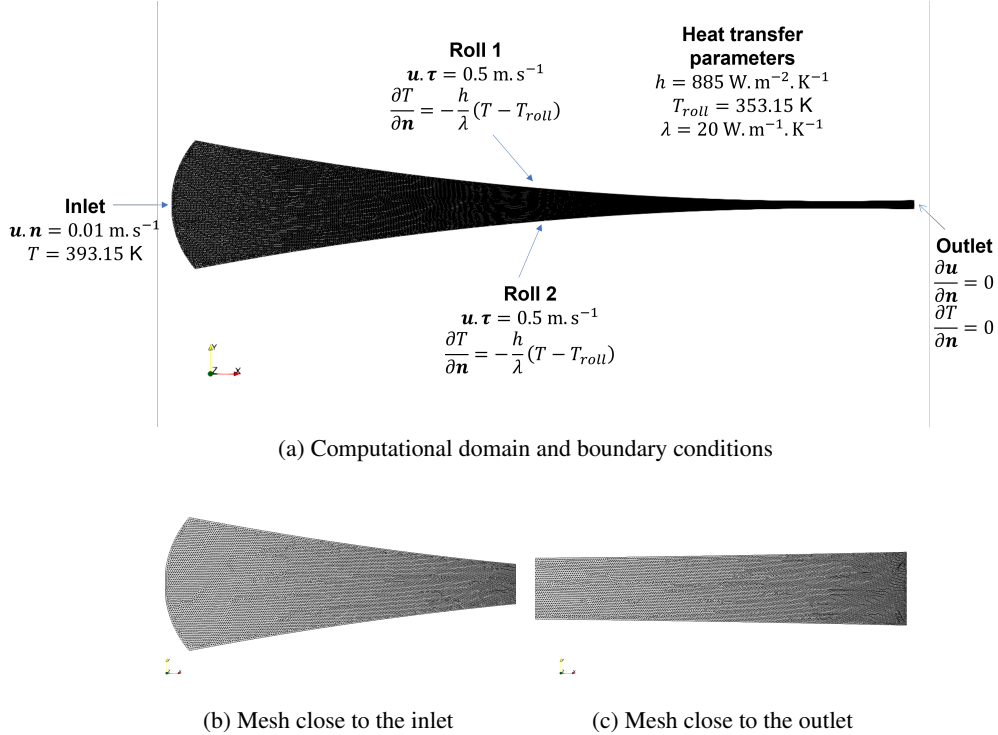


Figure 3: Sketch of the computational domain (the mesh is colored in black) with the velocity and temperature boundary conditions used in the reference finite element simulation:  $\mathbf{n}$  and  $\boldsymbol{\tau}$  denote respectively the normal and tangential vectors with respect to the corresponding boundary.

In our work, the errors are evaluated on two different evaluation meshes: the first one is a random mesh which is composed of points that are taken randomly uniformly inside the calender, while the second one is the finite element mesh, which provides us an *a priori* knowledge on the high gradient location. The numbers of points on these meshes are the same and equal to  $N = 163,596$ . The in-house solver gives us the high-fidelity solution at the points on the finite element mesh. To estimate the solution on the random mesh, we apply a linear interpolation using the HF data from the finite element mesh. Figure 4 shows the visualization of 1,000 random points on these meshes and Figure 5 illustrates the density of points on the line  $y = 0$  of each mesh. We point out that when the points are taken from the finite element mesh, the density of points is higher at the output than at the input of the calender. This is because the finite element mesh is refined to take into account the very thin gap between the rolls close to the domain outlet.

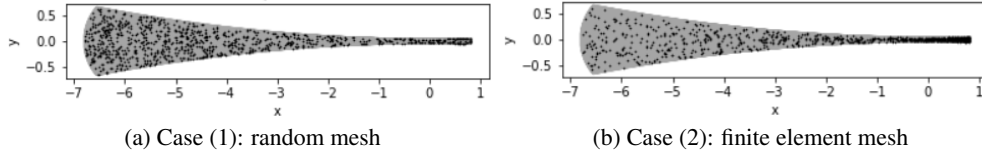


Figure 4: Visualization of 1,000 random points on the meshes: the black points represent the taken points.

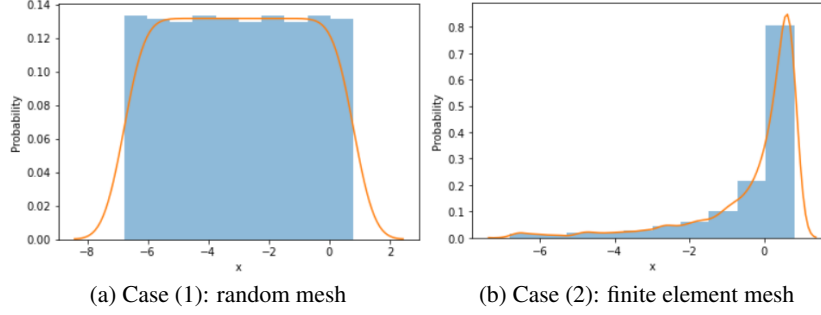


Figure 5: Density of points on the line  $y = 0$  for each mesh.

It is worth mentioning that before investigating the problem of calendering, PINNs implementation has been validated in a simple non-Newtonian laminar pipe flow configuration presented in Appendix A.

### 3.4 Inferring physical fields of interest from sensor measurements

In this section, we suppose that the boundary conditions of the problem are not completely defined, and we dispose of some measurements of the temperature from virtual sensors (in our case, coming from our finite element simulation). The goal is to infer the pressure, velocity, and temperature fields at all points in the domain. We note that here, no information on the pressure field is given, but only its gradient in the PDE residual is. Thus the pressure is only identifiable up to a constant.

#### 3.4.1 Impact of sensors location

We aim at studying the impact of the location of the sensors and the number of supervised points on the accuracy of PINNs prediction. For this purpose, we use PINNs with the spatial coordinates  $x, y$  as inputs and  $T, p, u_x, u_y$  as outputs and minimize the following cost function:

$$\begin{aligned}
 L &= L_{data} + L_{pde} \\
 &= \frac{1}{N_T} \sum_{i=1}^{N_T} \omega_T (\hat{T}^i - T^{i*})^2 + \frac{1}{N_f} \sum_{i=1}^{N_f} (\omega_1 e_1^2 + \omega_2 e_2^2 + \omega_3 e_3^2 + \omega_4 e_4^2)
 \end{aligned}$$

where  $\hat{T}$  are the prediction obtained by the neural network and  $T^*$  are the supervised data (measurements captured from the sensors) for the temperature. We note that there is no data for the velocity and the pressure in the cost function except their relation with the temperature given by the system of PDEs. The quantities  $e_1, e_2, e_3, e_4$  correspond to the dimensionless PDEs residuals defined in the equations (5), (6), (7). More precisely:

$$\begin{aligned}
 e_1 &= \frac{\partial}{\partial x} \left( 2\eta(\vec{u}, \hat{T}) \frac{\partial \hat{u}_x}{\partial x} \right) + \frac{\partial}{\partial y} \left( \eta(\vec{u}, \hat{T}) \left( \frac{\partial \hat{u}_x}{\partial y} + \frac{\partial \hat{u}_y}{\partial x} \right) \right) - \frac{\partial \hat{p}}{\partial x} \\
 e_2 &= \frac{\partial}{\partial x} \left( \eta(\vec{u}, \hat{T}) \left( \frac{\partial \hat{u}_x}{\partial y} + \frac{\partial \hat{u}_y}{\partial x} \right) \right) + \frac{\partial}{\partial y} \left( 2\eta(\vec{u}, \hat{T}) \frac{\partial \hat{u}_y}{\partial y} \right) - \frac{\partial \hat{p}}{\partial y} \\
 e_3 &= \frac{\partial \hat{u}_x}{\partial x} + \frac{\partial \hat{u}_y}{\partial y} \\
 e_4 &= \hat{u}_x \frac{\partial \hat{T}}{\partial x} + \hat{u}_y \frac{\partial \hat{T}}{\partial y} - \frac{1}{Pe} \left( \frac{\partial^2 \hat{T}}{\partial x^2} + \frac{\partial^2 \hat{T}}{\partial y^2} \right) - \frac{Br}{Pe} \eta(\vec{u}, \hat{T}) |\gamma(\vec{u})|^2
 \end{aligned}$$

The weight coefficients  $\omega_i$  for  $i \in \{T, 1, 2, 3, 4\}$  are pre-specified in our case (see below for their specific values). We suppose that there are sensors in the domain so that we can measure the temperature of the flow at these points. The placement of these sensors may be important as it may affect the inferred results. We study three cases of the sensors' placements as shown in Figure 6. In the first case (Figure 6a), the sensors are put randomly inside the calender. This is often the test case used in academic applications, but not always realistic in an industrial context. In the second case (Figure 6b), the sensors are put on two vertical lines located at the input and the output of the calender. In the third case (Figure 6c), the sensors are put randomly in the input zone of the calender. The last two cases are tested as they are often the case in industrial tasks.

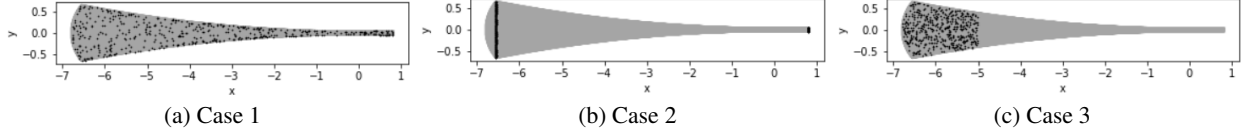


Figure 6: *Geometry of the rubber calender and the location of sensors*: the black points represent the location of sensors (or supervised points for the temperature).

To study the impact of the sensor's location on PINNs performance, we fix the number of measurements (supervised points) for the temperature  $N_T = 500$ . For the training of PINNs, the number of collocation points (unsupervised points) is  $N_f = 10,000$  and these points are generated randomly on the finite element mesh, which provides an *a priori* knowledge on high gradient location (see Figure 4b). We use a feedforward network of 5 layers and 100 neurons in each layer. To minimize the loss function, we use Adam optimizer with 100,000 epochs with the learning rate  $lr = 10^{-3}$ , 200,000 epochs with the learning rate  $lr = 10^{-4}$  and 50,000 epochs with  $lr = 10^{-5}$ . For the weight coefficients, we fix  $\omega_1 = \omega_2 = \omega_3 = \omega_4 = 1$  and  $\omega_T = \frac{N_T}{\sum_{i=1}^{N_T} (T^{i*})^2}$ . By putting these weights, we aim at minimizing the relative errors between the PINNs prediction and solution for the supervised points in the cost function, instead of minimizing the absolute errors as in the vanilla PINNs.

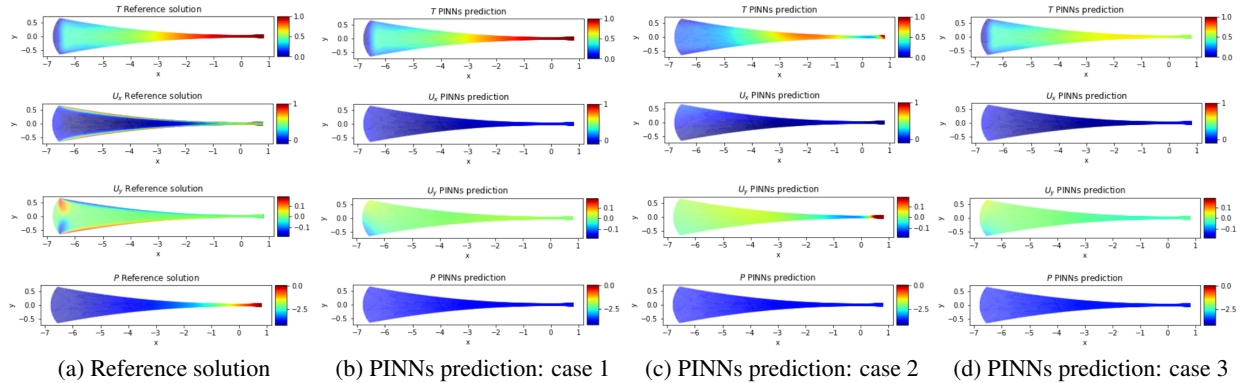


Figure 7: *Reference solution and PINNs predictions in different scenarios of the location of sensors*: from top to bottom: the solution for the temperature, the velocity components and the pressure, respectively.

Figure 7 illustrates the visual comparison between the reference solution and PINNs prediction in different scenarios of the location of sensors. We observe that in all three cases, PINNs are only able to approximate accurately the temperature in the zones where there are sensors and fail to predict the velocity and pressure. This performance demonstrates that the information of the temperature is not sufficient to guarantee a unique solution for the velocity and the pressure fields.

To make sure that the problem has a unique solution, we take in addition the knowledge of the velocity boundary conditions. Moreover, since the supervised points for the temperature are only available at some specific location, PINNs, as other deep learning methods, will have difficulty to extrapolating the values of the temperature at points far from the sensors. Thus we also provide PINNs with the information of the temperature on the roll boundaries only. We



note that when the sensors are distributed as in case 1 (Figure 4a), the learning points for the temperature on the roll boundaries are not necessary. The cost function in PINNs now becomes:

$$\begin{aligned}
 L &= L_{data} + L_{pde} + L_{bc} \\
 &= \frac{1}{N_T} \sum_{i=1}^{N_T} \omega_T (\hat{T}^i - T^{i*})^2 + \frac{1}{N_f} \sum_{i=1}^{N_f} (\omega_1 e_1^2 + \omega_2 e_2^2 + \omega_3 e_3^2 + \omega_4 e_4^2) \\
 &\quad + \frac{1}{N_{rolls}} \sum_{i=1}^{N_{rolls}} (\omega_{T_{rolls}} (\hat{T}^{rolls,i} - T^{rolls,i*})) + \frac{1}{N_{bc}} \sum_{i=1}^{N_{bc}} \left( \omega_{u_x^{bc}} (\hat{u}_x^{bc,i} - u_x^{bc,i*})^2 + \omega_{u_y^{bc}} (\hat{u}_y^{bc,i} - u_y^{bc,i*})^2 \right)
 \end{aligned}$$

where  $T^{rolls*}$  denotes the values of the temperature on the rolls and  $u_x^{bc*}, u_y^{bc*}$  denotes the components of the velocity on the four boundaries of the calender. For the weight coefficients, we fix  $\omega_1 = \omega_2 = \omega_3 = \omega_4 = 1$ ,  $\omega_T = \frac{N_T}{\sum_{i=1}^{N_T} (T^{i*})^2}$ ,

$\omega_{T_{rolls}} = \frac{N_{rolls}}{\sum_{i=1}^{N_{rolls}} (T^{rolls,i*})^2}$ ,  $\omega_{u_x^{bc}} = \frac{100N_{bc}}{\sum_{i=1}^{N_{bc}} (u_x^{bc,i*})^2}$  and  $\omega_{u_y^{bc}} = \frac{10N_{bc}}{\sum_{i=1}^{N_{bc}} (u_y^{bc,i*})^2}$ . Here we still minimize the relative errors between the prediction and the solution at the learning points, but we put more important weights on the boundary condition for the velocity. Figure 8 presents the performance of PINNs in this case. We see that PINNs are capable to predict accurately the physical fields even in the case where there are only sensors at the input and output lines of the calender (case 2). However, when there are only sensors at the input zone (case 3), PINNs are able to fit the boundary condition for the temperature and the velocity, but still fail to approximate accurately the solution at the output of the calender.

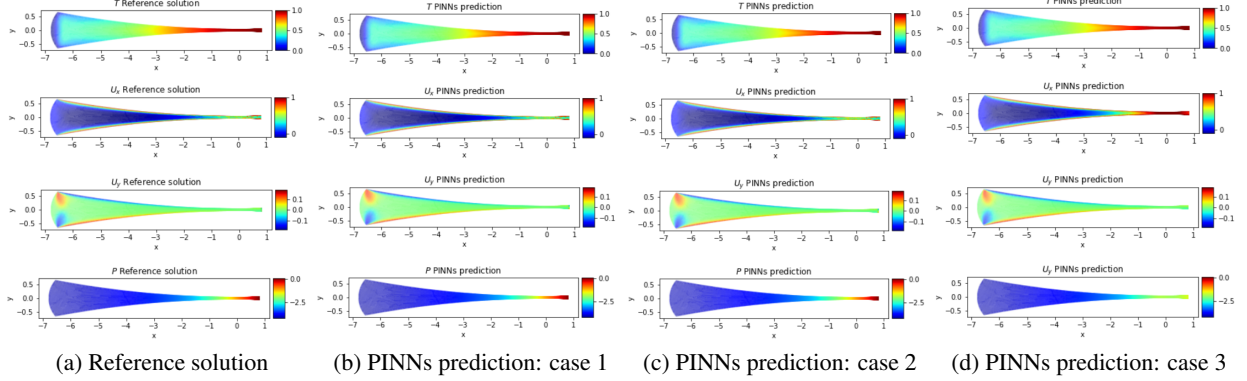


Figure 8: Reference solution and PINNs prediction when using in addition the boundary condition for the velocity and the temperature as learning data.

Next, we study two different cases for the distribution of collocation points: in the first case, these points are generated randomly inside the domain while in the second case, they are generated randomly on the finite element mesh. An example of the visualization of these collocation points can be seen in Figure 4. Table 1 summarizes the performance of PINNs in terms of relative  $\mathcal{L}^2$  errors compared with the reference solution. These errors are evaluated on two different meshes: the random mesh and the finite element mesh. It can be observed that, in both different cases of evaluation mesh, using the collocation points randomly taken from the finite element mesh allows PINNs to give a much better precision than using the points randomly taken inside the domain. We also notice that, when the errors are evaluated on the finite element mesh which is much finer at the output, the error of the prediction at the output gives a more important weight than the one at the input in the final accuracy. This remark can be seen clearly in case 3 of the placement of the sensors where we obtain a very high relative error for  $u_x$  (up to 85% when evaluated on the finite element mesh and 45% on the random mesh), however, PINNs only fail to predict precisely the solution at the output of the calender (which is reasonable as we only have supervised points at the input).

		$\epsilon_T$		$\epsilon_{u_x}$		$\epsilon_{u_y}$		$\epsilon_p$	
		(1)	(2)	(1)	(2)	(1)	(2)	(1)	(2)
Rand.	Case 1	1.42e-01	<b>7.79e-02</b>	1.02e-01	<b>7.97e-02</b>	<b>1.81e-01</b>	2.27e-01	4.12e-02	<b>2.03e-03</b>
	Case 2	1.15e-01	<b>9.42e-02</b>	4.77e-01	<b>7.08e-02</b>	1.43e-01	<b>1.41e-01</b>	7.69e-02	<b>3.95e-02</b>
	Case 3	1.38e-01	3.22e-02	4.84e-01	4.53e-01	1.02e-01	8.81e-02	2.10e-01	7.11e-02
FE	Case 1	4.68e-02	<b>2.66e-02</b>	1.51e-01	<b>2.25e-02</b>	2.21e-01	<b>2.20e-01</b>	8.28e-02	<b>2.37e-03</b>
	Case 2	4.54e-02	<b>3.34e-02</b>	3.78e-01	<b>5.26e-02</b>	3.83e-01	<b>2.00e-01</b>	2.20e-02	<b>7.68e-03</b>
	Case 3	4.76e-02	1.92e-02	9.29e-01	8.85e-01	2.14e-01	2.08e-01	2.56e-01	2.03e-01

Table 1: *Relative  $\mathcal{L}^2$  error between the reference solution and the predictions by PINNs in different scenarios of sensors' placement. We evaluate the errors on two different meshes: the random mesh (Rand.) and the finite element mesh (FE). We also compare two cases of the collocation points' distribution: (1) these points are taken randomly on the random mesh. (2) these points are taken randomly on the finite element mesh. The results highlighted in bold are the ones that provide satisfying predictions visually and numerically.*

### 3.4.2 Impact of noisy measurements:

In realistic circumstances, the measurements captured from the sensors are always corrupted with some noise. We investigate here the impact of noisy measurements on the quality of PINNs prediction. To this end, we only consider the case where there are two lines of sensors that are put at the input and output of the calender (case 2). We generate the noise as uncorrelated Gaussian noise for the supervised data. We vary the level of noise to verify the effectiveness of PINNs when dealing with noisy measurements. PINNs configuration is the same as the cases before except that now we train with more epochs. More precisely, we use Adam optimizer with 50,000 epochs with the learning rate  $lr = 10^{-3}$ , 200,000 epochs with the learning rate  $lr = 10^{-4}$  and 300,000 epochs with  $lr = 10^{-5}$ . Figure 9 compares visually the performance of PINNs with different levels of noise. We see that PINNs are able to accurately predict all the physical fields whether the training data are corrupted with noise or not. Table 2 illustrates in more detail the quality of PINNs prediction in terms of relative  $\mathcal{L}^2$  errors with the reference solution. These errors are evaluated on the finite element mesh. It is clear that the accuracy of PINNs prediction remains robust even when the supervised data are corrupted with 10% noise.

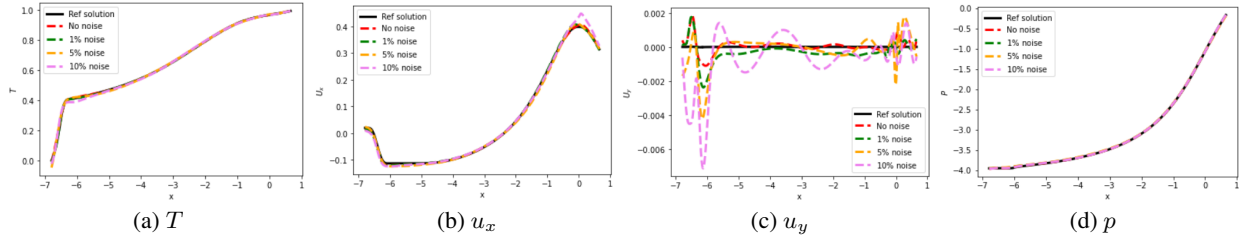


Figure 9: *Reference solution and PINNs prediction for the physical fields at the line  $y = 0$ .*

	$\epsilon_T$	$\epsilon_{u_x}$	$\epsilon_{u_y}$	$\epsilon_p$
0% noise	1.15e-02	3.41e-02	1.83e-01	3.60e-03
1% noise	1.49e-02	4.16e-02	2.23e-01	4.52e-03
5% noise	1.58e-02	5.01e-02	2.42e-01	6.85e-03
10% noise	1.88e-02	5.23e-02	2.98e-01	7.09e-03

Table 2: *Relative  $\mathcal{L}^2$  error between the reference solution and the predictions by PINNs with different level of noise.*

### 3.5 Identifying unknown physical parameters

In the industrial context, it is often the case that some physical parameters are not defined but we observe some measurements of the solution. These problems are referred to as inverse problems, which are difficult to be solved in practice using traditional methods. In this section, we aim to demonstrate the capability of PINNs of identifying an unknown physical parameter (namely the thermal conductivity of the rubber  $\lambda$ ) from some observed measurements. To this end, we suppose that we do not know the value of the thermal conductivity  $\lambda$  in the temperature equation (Eq. (4)) but we dispose of some measurements for the temperature and the velocity (which may be noisy) from the

sensors. We note that the conductivity is essential to define the value of the Péclet number and Brinkman number in the dimensionless PDE. Hence, we use PINNs to define these two unknown parameters in the dimensionless PDE and then deduce the value of the conductivity. We note that, in this case, the only considered PDE is the equation of conservation of energy (Eq. (7)) as the conductivity only appears in this equation. We study the impact of the sensors' location and also the impact of noisy measurements on PINNs identification capability.

In identification problems, the unknown parameters (Péclet number and Brinkman number in our case) are considered as network parameters that will be learned during the training process. As for the case before, we use PINNs with the spatial coordinates  $x, y$  as inputs and  $T, p, u_x, u_y$  as outputs and minimize the following cost function:

$$L = L_{data} + L_{pde}$$

$$= \frac{\omega_T}{N_T} \sum_{i=1}^{N_T} (\hat{T}^i - T^{i*})^2 + \frac{1}{N_U} \sum_{i=1}^{N_U} \left( \omega_{u_x} (\hat{u}_x^i - u_x^{i*})^2 + \omega_{u_y} (\hat{u}_y^i - u_y^{i*})^2 \right) + \frac{1}{N_f} \sum_{i=1}^{N_f} \omega_4 e_4^2$$

where  $e_4$  is the dimensionless PDE residual corresponding to Eq. (7). The weight coefficients are fixed as follows:  $\omega_T = \frac{N_T}{\sum_{i=1}^{N_T} (T^{i*})^2}$ ,  $\omega_{u_x} = \frac{N_U}{\sum_{i=1}^{N_U} (u_x^{i*})^2}$  and  $\omega_{u_y} = \frac{N_U}{\sum_{i=1}^{N_U} (u_y^{i*})^2}$  and  $\omega_4 = 1$ . We note that here, no information on the boundary is given.

As before, the location of sensors may have an important impact on the performance of PINNs. To verify this, we consider three cases as shown in Figure 6. First, we suppose that all the supervised measurements are high-fidelity (*i.e.* no noisy measurements). For the training of PINNs, the number of measurements captured from the sensors for the temperature and the velocity is  $N_T = N_U = 500$ . The number of collocation points is  $N_f = 10,000$  and these points are randomly taken from the finite element mesh. We use a feedforward network of 5 layers and 100 neurons in each layer. To minimize the loss function, we use Adam optimizer with 50,000 epochs with the learning rate  $lr = 10^{-3}$ , 200,000 epochs with the learning rate  $lr = 10^{-4}$  and 150,000 epochs with  $lr = 10^{-5}$ .

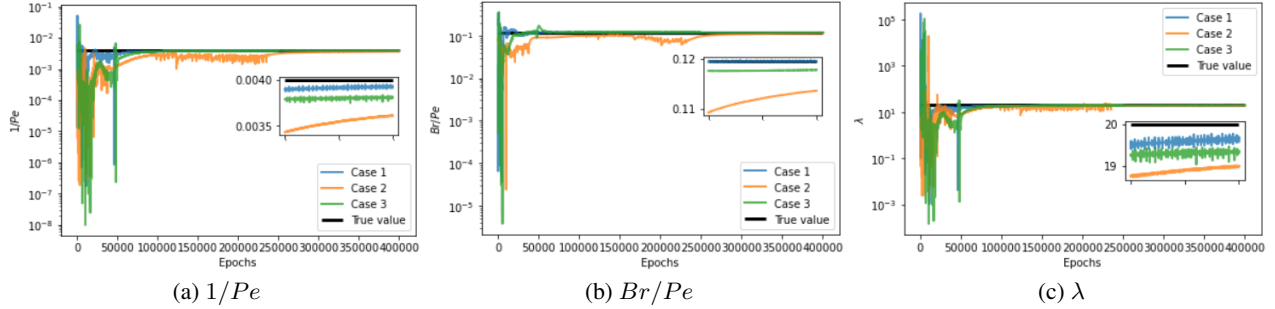


Figure 10: Prediction for unknown parameters during the training process while considering different cases of the location of sensors. The small plots show the results at the last 100,000 epochs.

	$1/Pe$	$Br/Pe$	$\lambda$
High-fidelity model	4.00e-03	1.20e-01	2.00e+01
Case 1	3.93e-03	1.20e-01	1.97e+01
Case 2	3.64e-03	1.14e-01	1.90e+01
Case 3	3.81e-03	1.18e-01	1.94e+01

Table 3: Prediction for unknown parameters at the end of PINNs training process

Figure 10 shows the prediction values for  $1/Pe$ ,  $Br/Pe$  and  $\lambda$  during the process. We note that the value of  $\lambda$  is inferred from the values of  $1/Pe$  and  $Br/Pe$ . In all cases, the predictions of PINNs for PDEs parameters converge to the true values. Table 3 presents the final prediction for these parameters at the end of the training process. We see that the case 1 (Figure 6a) and case 3 of the location of sensors (Figure 6c) provide a slightly better performance than the case 2 (Figure 6b). However, it is remarkable that in case 2, with only two lines of sensors at the input and output of the calender, PINNs are still capable of approximating the unknown parameters with high accuracy.

Next, we investigate the impact of noisy measurements on the performance of PINNs. For this purpose, we only consider case 3 where the sensors are located as shown in Figure 6c. We generate the noise as uncorrelated Gaussian

noise. We vary the number of supervised points and the level of noise to verify the effectiveness of PINNs when dealing with noisy measurements. We use the same configuration as the case before for PINNs, however, we increase the number of epochs for the training process. More precisely, we use Adam optimizer with 50,000 epochs with the learning rate  $lr = 10^{-3}$ , 200,000 epochs with the learning rate  $lr = 10^{-4}$  and 300,000 epochs with  $lr = 10^{-5}$ .

	$1/Pe$	$Br/Pe$	$\lambda$
High-fidelity model	4.00e-03	1.20e-01	2.00e+01
0% noise	3.94e-03	1.19e-01	1.97e+01
1% noise	3.87e-03	1.17e-01	1.94e+01
5% noise	3.81e-03	1.16e-01	1.90e+01
10% noise	3.72e-03	1.16e-01	1.86e+01

Table 4: Prediction for unknown parameters at the end of PINNs training process while considering different levels of noisy measurements in supervised data

Table 4 summarizes the performance of PINNs in case of noisy measurements. The errors are evaluated on the finite element mesh. We see that, even though the accuracy decreases when the level of noise increases, PINNs are still able to approximate the unknown parameters with high accuracy even when the training data are corrupted with 10% noise.

## 4 Conclusion

In this study, we demonstrated the interest of using Physics-Informed Neural Networks (PINNs) for the modeling of the rubber calendering process. As far as our knowledge, this is the first time PINNs are applied to solve a non-Newtonian fluid thermo-mechanical problem. PINNs have shown a great capability to infer all the physical fields without using any supervised data for the velocity and the pressure fields but taking some knowledge on the boundary for the velocity and the temperature. We demonstrated an important impact of the placement of the sensors (or the position of supervised data) on the prediction quality of PINNs. We investigated the effect of the distribution of collocation points on the prediction quality. We concluded that training PINNs with the collocation points that were taken randomly on a finite element mesh (which provides an *a priori* knowledge on high gradient location) provides much better models than training with the collocation points that were taken randomly inside the domain. We also tested the robustness of PINNs when dealing with noisy measurements. The results demonstrated that when training with sufficient epochs, PINNs are capable of predicting the reference solution with the same accuracy as when using high-fidelity data. Concerning the identification problem, we showed that with any case of the location of sensors, PINNs are able to approximate the unknown thermal conductivity. We also demonstrated that even when the supervised data are corrupted with noise, the quality of PINNs prediction still remains accurate as expected.

Through our work, it can be seen that there are many opportunities for further research. We observed that in some cases, PINNs are able to give a satisfying performance visually, but however still give a very high relative error, which is evaluated either on a finite element mesh or on a random mesh, compared to the reference solution. This suggests to examine the accuracy of PINNs on more appropriate quantities which present some expected physical properties. We can think of methods of model reduction such as Proper Orthogonal Decomposition (POD) or Dynamic Mode Decomposition (DMD) to extract the most important modes (in terms of energy or dynamic), and then calculate the error of PINNs on these modes. Another perspective is to combine PINNs and reduced-order methods to improve learning efficiency. We aim to purchase these lines of research in our future work.

## Acknowledgements

T.N.K. Nguyen is funded by Michelin and CEA through the Industrial Data Analytics and Machine Learning chair of ENS Paris-Saclay. In addition, the authors would like to thank Christophe Millet for fruitful discussions.

## Conflict of interest

The authors declare no conflict of interest.

## References

- [1] Maziar Raissi, Paris Perdikaris, and George E Karniadakis. Physics-informed neural networks: A deep learning framework for solving forward and inverse problems involving nonlinear partial differential equations. *Journal of Computational Physics*, 378:686–707, 2019.
- [2] Justin Sirignano and Konstantinos Spiliopoulos. Dgm: A deep learning algorithm for solving partial differential equations. *Journal of computational physics*, 375:1339–1364, 2018.
- [3] Christopher Rackauckas, Yingbo Ma, Julius Martensen, Collin Warner, Kirill Zubov, Rohit Supekar, Dominic Skinner, Ali Ramadhan, and Alan Edelman. Universal differential equations for scientific machine learning. *arXiv preprint arXiv:2001.04385*, 2020.
- [4] Zongyi Li, Nikola Kovachki, Kamyar Azizzadenesheli, Burigede Liu, Kaushik Bhattacharya, Andrew Stuart, and Anima Anandkumar. Fourier neural operator for parametric partial differential equations. *arXiv preprint arXiv:2010.08895*, 2020.
- [5] Han Gao, Luning Sun, and Jian-Xun Wang. Phygeonet: physics-informed geometry-adaptive convolutional neural networks for solving parameterized steady-state pdes on irregular domain. *Journal of Computational Physics*, 428:110079, 2021.
- [6] Yin hao Zhu, Nicholas Zabaras, Phaedon-Stelios Koutsourelakis, and Paris Perdikaris. Physics-constrained deep learning for high-dimensional surrogate modeling and uncertainty quantification without labeled data. *Journal of Computational Physics*, 394:56–81, 2019.
- [7] Luning Sun and Jian-Xun Wang. Physics-constrained bayesian neural network for fluid flow reconstruction with sparse and noisy data. *Theoretical and Applied Mechanics Letters*, 10(3):161–169, 2020.
- [8] Luning Sun, Han Gao, Shaowu Pan, and Jian-Xun Wang. Surrogate modeling for fluid flows based on physics-constrained deep learning without simulation data. *Computer Methods in Applied Mechanics and Engineering*, 361:112732, 2020.
- [9] Lu Lu, Xuhui Meng, Zhiping Mao, and George Em Karniadakis. Deepxde: A deep learning library for solving differential equations. *SIAM Review*, 63(1):208–228, 2021.
- [10] Sifan Wang, Yujun Teng, and Paris Perdikaris. Understanding and mitigating gradient pathologies in physics-informed neural networks. *arXiv preprint arXiv:2001.04536*, 2020.
- [11] Ameya D Jagtap, Kenji Kawaguchi, and George Em Karniadakis. Adaptive activation functions accelerate convergence in deep and physics-informed neural networks. *Journal of Computational Physics*, 404:109136, 2020.
- [12] Levi McClenny and Ulisses Braga-Neto. Self-adaptive physics-informed neural networks using a soft attention mechanism. *arXiv preprint arXiv:2009.04544*, 2020.
- [13] Georgios Kissas, Yibo Yang, Eileen Hwuang, Walter R Witschey, John A Detre, and Paris Perdikaris. Machine learning in cardiovascular flows modeling: Predicting arterial blood pressure from non-invasive 4d flow mri data using physics-informed neural networks. *Computer Methods in Applied Mechanics and Engineering*, 358:112623, 2020.
- [14] Alexandre M Tartakovsky, C Ortiz Marrero, Paris Perdikaris, Guzel D Tartakovsky, and David Barajas-Solano. Physics-informed deep neural networks for learning parameters and constitutive relationships in subsurface flow problems. *Water Resources Research*, 56(5):e2019WR026731, 2020.
- [15] QiZhi He, David Barajas-Solano, Guzel Tartakovsky, and Alexandre M Tartakovsky. Physics-informed neural networks for multiphysics data assimilation with application to subsurface transport. *Advances in Water Resources*, 141:103610, 2020.
- [16] Oliver Hennigh, Susheela Narasimhan, Mohammad Amin Nabian, Akshay Subramaniam, Kaustubh Tangsali, Zhiwei Fang, Max Rietmann, Wonmin Byeon, and Sanjay Choudhry. Nvidia simnet™: An ai-accelerated multi-physics simulation framework. In *International Conference on Computational Science*, pages 447–461. Springer, 2021.
- [17] Shengze Cai, Zhicheng Wang, Sifan Wang, Paris Perdikaris, and George Karniadakis. Physics-informed neural networks (pinns) for heat transfer problems. *Journal of Heat Transfer*, 2021.
- [18] Maziar Raissi, Alireza Yazdani, and George Em Karniadakis. Hidden fluid mechanics: Learning velocity and pressure fields from flow visualizations. *Science*, 367(6481):1026–1030, 2020.
- [19] Chengping Rao, Hao Sun, and Yang Liu. Physics-informed deep learning for incompressible laminar flows. *Theoretical and Applied Mechanics Letters*, 10(3):207–212, 2020.

- [20] Brandon Reyes, Amanda A Howard, Paris Perdikaris, and Alexandre M Tartakovsky. Learning unknown physics of non-newtonian fluids. *Physical Review Fluids*, 6(7):073301, 2021.
- [21] Shengze Cai, Zhicheng Wang, Frederik Fuest, Young Jin Jeon, Callum Gray, and George Em Karniadakis. Flow over an espresso cup: inferring 3-d velocity and pressure fields from tomographic background oriented schlieren via physics-informed neural networks. *Journal of Fluid Mechanics*, 915, 2021.
- [22] Shengze Cai, Zhiping Mao, Zhicheng Wang, Minglang Yin, and George Em Karniadakis. Physics-informed neural networks (pinns) for fluid mechanics: A review. *arXiv preprint arXiv:2105.09506*, 2021.
- [23] Xiaowei Jin, Shengze Cai, Hui Li, and George Em Karniadakis. Nsfnets (navier-stokes flow nets): Physics-informed neural networks for the incompressible navier-stokes equations. *Journal of Computational Physics*, 426:109951, 2021.
- [24] Zhiping Mao, Ameya D Jagtap, and George Em Karniadakis. Physics-informed neural networks for high-speed flows. *Computer Methods in Applied Mechanics and Engineering*, 360:112789, 2020.
- [25] Mohammadamin Mahmoudabadbozchelou, George Em Karniadakis, and Safa Jamali. nn-pinns: Non-newtonian physics-informed neural networks for complex fluid modeling. *Soft Matter*, 18(1):172–185, 2022.
- [26] Sifan Wang, Xinling Yu, and Paris Perdikaris. When and why pinns fail to train: A neural tangent kernel perspective. *arXiv preprint arXiv:2007.14527*, 2020.
- [27] Atilim Gunes Baydin, Barak A Pearlmutter, Alexey Andreyevich Radul, and Jeffrey Mark Siskind. Automatic differentiation in machine learning: a survey. *Journal of machine learning research*, 18, 2018.
- [28] MEF++. <https://fr.wikipedia.org/wiki/mef>
- [29] R Gu  nette, A Fortin, J Labb  , and JP Marcotte. Iterative solvers for quadratic discretizations of the generalized stokes problem. *International journal for numerical methods in fluids*, 44(7):695–720, 2004.

## A Validation of PINNs with analytical solution

In this section, we provide the comparison of PINNs and the analytical solution in a pipe (Figure 11), using the same Stokes equation but without thermal coupling. The considered PDE is written as follows:

$$\begin{aligned} \nabla \cdot (2\eta(\vec{u})\vec{\epsilon}(\vec{u})) - \vec{\nabla} p &= \vec{0} \\ \nabla \cdot \vec{u} &= 0 \end{aligned}$$

where the generalized strain rate  $\gamma(\vec{u}) = \sqrt{2 \sum_{i,j} \bar{\epsilon}_{i,j}^2}$  and the dynamic viscosity:  $\eta(\vec{u}) = K|\gamma(\vec{u})|^{n-1}$ . We set the boundary condition as follows: the velocity of the fluid at the wall is supposed to be zero (no-slip condition), and the input flow rate  $Q$  is fixed.

To calculate the analytical solution, we use the cylindrical coordinates  $(r, \theta, z)$ . We suppose that the flow is axisymmetric ( $\frac{\partial}{\partial \theta} = 0$ ), and we search for a solution  $\vec{u} = (u_r, u_\theta, u_z)$  where  $u_r = 0, u_\theta = 0$ .

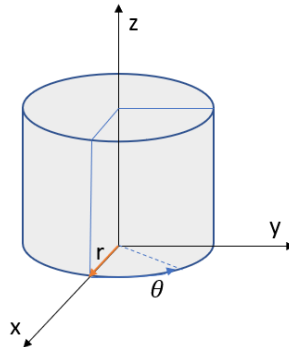


Figure 11: Sketch of the pipe configuration

By re-writting the PDE in cylindrical coordinates, the equation of conservation of mass gives us:

$$\nabla \cdot \vec{u} = 0 \Leftrightarrow \frac{\partial u_z}{\partial z} = 0$$

And the equation of conservation of energy gives us:

$$\begin{aligned} & \nabla \cdot (2\eta(\vec{u})\vec{\epsilon}(\vec{u})) - \vec{\nabla} p = \vec{0} \\ \Leftrightarrow & \begin{cases} \frac{\partial p}{\partial r} = 0 \\ \frac{\partial p}{\partial \theta} = 0 \\ \frac{1}{r} \frac{\partial}{\partial r} (r\eta(\vec{u}) \frac{\partial u_z}{\partial r}) - \frac{\partial p}{\partial z} = 0 \end{cases} \end{aligned}$$

In the last obtained equation, by taking the integral three times and using the boundary condition  $u_z = 0$  at  $r = R$ , we get:

$$u_z = \left(-\frac{\Delta P}{LK} \frac{1}{2}\right)^{1/n} \frac{n}{n+1} \left(R^{\frac{n+1}{n}} - r^{\frac{n+1}{n}}\right)$$

To calculate  $u_z$  explicitly, we use the analytical formulation of the pressure difference along the pipe length:

$$\Delta P = -2 \left( \frac{Q(\frac{1}{n} + 3)}{\pi R^3} \right)^n L \frac{K}{R}$$

where  $L$  is the length of the pipe and  $Q$  the flow rate.

We now use PINNs to solve this problem by assuming that the boundary condition is unknown but we dispose of the solution at some points in the pipe. The goal is to infer the pressure and the velocity at all points in the domain. Due to the symmetry of the problem, we only consider a quarter of the pipe.

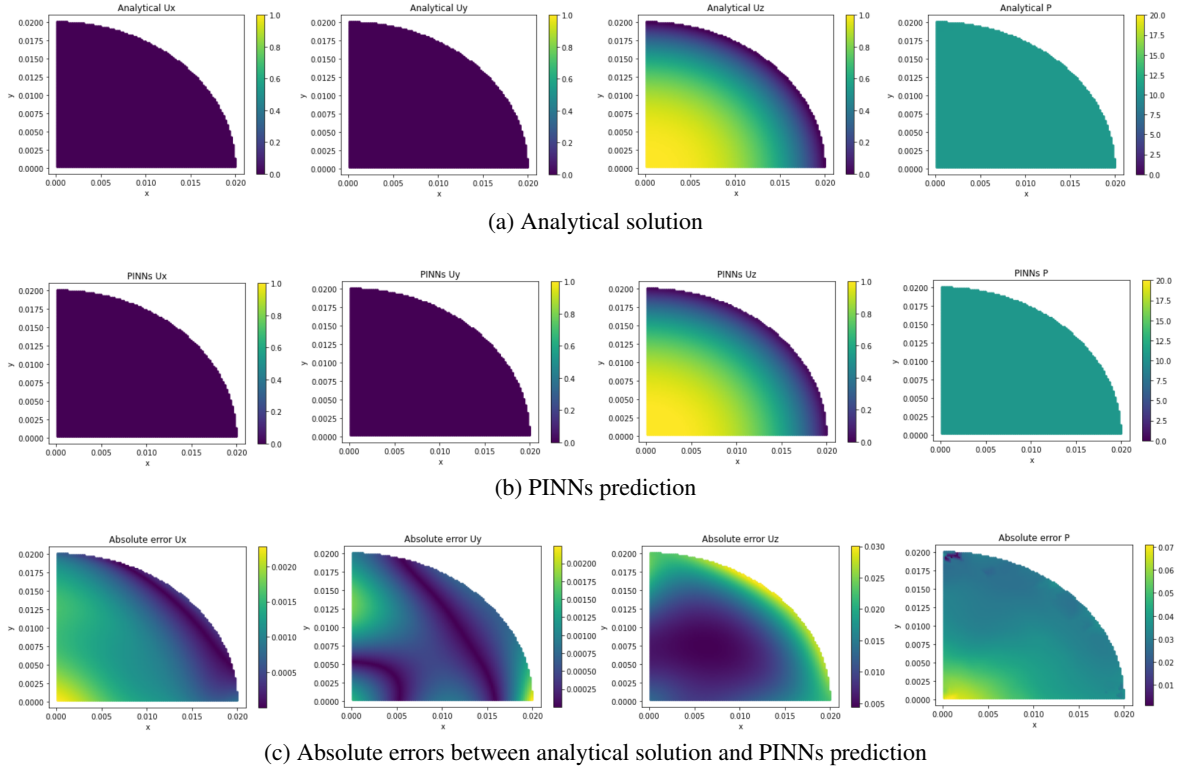


Figure 12: Visualization of analytical solution and PINNs prediction at the plan  $z = cst$ : from left to right: the velocity components ( $u_x, u_y, u_z$ ) and the pressure  $p$ .

We fix the number of supervised points for the velocity as  $N_U = 5,000$  and the number of collocation points is  $N_f = 20,000$ . We suppose that both the supervised points and collocation points are randomly distributed in the

pipe. We use a feedforward network of 5 layers and 100 neurons in each layer. To minimize the loss function, we use Adam optimizer with 20,000 epochs with the learning rate  $lr = 10^{-3}$ . The loss function is defined similarly to the loss function in section 3.4. Figure 12 presents the comparison of the analytical solution and PINNs prediction at the plan  $z = cst$ . The relative  $\mathcal{L}^2$  errors at all points in the pipe for  $u_z$  and  $P$  are 2.59e-02 and 1.87e-02, respectively.